Lab on a Chip

PAPER

View Article Online
View Journal | View Issue

Cite this: *Lab Chip*, 2022, **22**, 4905

A dental implant-on-a-chip for 3D modeling of host–material–pathogen interactions and therapeutic testing platforms†

Atul Dhall, [a] Jun Ying Tan,[b] Min Jun Oh,[ac] Sayemul Islam,[df] Jungkwun Kim,*[be] Albert Kim *[df] and Geelsu Hwang *[ag]

Received 19th August 2022,
Accepted 7th November 2022

DOI: 10.1039/d2lc00774f

rsc.li/loc

The precise spatiotemporal control and manipulation of fluid dynamics on a small scale granted by lab-on-a-chip devices provide a new biomedical research realm as a substitute for *in vivo* studies of host–pathogen interactions. While there has been a rise in the use of various medical devices/implants for human use, the applicability of microfluidic models that integrate such functional biomaterials is currently limited. Here, we introduced a novel dental implant-on-a-chip model to better understand host–material–pathogen interactions in the context of peri-implant diseases. The implant-on-a-chip integrates gingival cells with relevant biomaterials – keratinocytes with dental resin and fibroblasts with titanium while maintaining a spatially separated co-culture. To enable this co-culture, the implant-on-a-chip's core structure necessitates closely spaced, tall microtrenches. Thus, an SU-8 master mold with a high aspect-ratio pillar array was created by employing a unique backside UV exposure with a selective optical filter. With this model, we successfully replicated the morphology of keratinocytes and fibroblasts in the vicinity of dental implant biomaterials. Furthermore, we demonstrated how photobiomodulation therapy might be used to protect the epithelial layer from recurrent bacterial challenges (~3.5-fold reduction in cellular damage *vs.* control). Overall, our dental implant-on-a-chip approach proposes a new microfluidic model for multiplexed host–material–pathogen investigations and the evaluation of novel treatment strategies for infectious diseases.

Introduction

Microfluidics has been embraced by various fields within biomedical research.[1,2] Utilizing fabrication technologies from the microelectromechanical systems (MEMS) and semiconductor industries[2] enables precise control and manipulation of fluids at the submillimeter scale, bringing several distinct advantages from conventional approaches. For example, it requires substantially smaller sample volumes, enables high-throughput analyses, and provides greater control over the spatiotemporal fluid dynamics at a lower cost. Since these advantages translate well in biomedical research, a microfluidic setting is often chosen to model microenvironments, intended to substitute *in vivo* studies; a highly engineered microfluidics platform, organ-on-a-chip, is a noteworthy approach in the recent trend.[3]

When mimicking cellular microenvironments, a co-culture model that depicts physiologically relevant behaviors is a better approach than simplistic 2D monoculture systems.[4] Indeed, several organ-on-a-chip systems already provided improved replication of tissue functionality in comparison to conventional 2D and 3D static cell culture systems. These include notable examples like gut-on-a-chip,[5] liver-on-a-chip,[6] lung-on-a-chip,[7] bone-marrow-on-a-chip,[8] and eye-on-a-chip.[9] Additional prominent examples of on-chip systems include contact-lens-on-a-chip[10] and a foreign-body-response-on-a-chip.[11] Despite such innovations in microfluidics with mimicking various parts of the human body and the rise in

[a] *Department of Preventive and Restorative Sciences, School of Dental Medicine, University of Pennsylvania, Philadelphia, PA 19104, USA. E-mail: geelsuh@upenn.edu*
[b] *Department of Electrical and Computer Engineering, Kansas State University, Manhattan, KS 66506, USA*
[c] *Department of Chemical and Biomolecular Engineering, School of Engineering and Applied Sciences, University of Pennsylvania, Philadelphia, PA 19104, USA*
[d] *Department of Electrical and Computer Engineering, Temple University, Philadelphia, PA 19122, USA*
[e] *Department of Electrical Engineering, University of North Texas, Denton, TX 76203, USA. E-mail: jungkwun.kim@unt.edu*
[f] *Department of Medical Engineering, University of South Florida, Tampa, FL 33620, USA. E-mail: akim1@usf.edu*
[g] *Center for Innovation & Precision Dentistry, School of Dental Medicine, School of Engineering and Applied Sciences, University of Pennsylvania, Philadelphia, PA 19104, USA*

† Electronic supplementary information (ESI) available. See DOI: https://doi.org/10.1039/d2lc00774f

the use of a range of medical devices (or implants) for human use, the applicability of microfluidic models that resemble the complex microenvironmental interactions among the host, material, and pathogen is currently limited.

Due to the marsupialization of the skin epithelium along with implants, the implant serves as a major conduit for pathogen mobilization.[12] In the absence of a robust tissue barrier, organisms populating the implant can penetrate through the epidermis into the soft tissue and ultimately invade bone trabeculae. Since the skin interface is the common failure point, it is increasingly important to better understand host–material–pathogen interactions. For example, the oral mucosal barrier is a layered tissue with an active microbiome that is heavily colonized and often subjected to repetitive trauma.[13] Such microbial challenges to peri-implant soft tissue are one of the major components associated with the pathogenesis of peri-implant diseases.[14,15] Notably, the prevalence of such osseointegrated dental implants in the US is projected to reach as high as 23% by 2026 with an aging population,[16] elevating implant complications due to the popularity of dental implants.[17,18] As establishing a peri-implant soft tissue seal to the implant to prevent its failure from microbial insult is critical,[19] there is considerable interest in studying host–material–pathogen interactions in the oral environment. However, no microfluidic models are presently available for studying the behaviors of the peri-implant soft tissue microenvironment in relation to biomaterials, such as dental resin and titanium (*i.e.*, two major components of dental implants). Given the advantages of microfluidic co-culture models, the rise in modular microfluidics, and the past successes of organ-on-a-chip systems, a microfluidic model to replicate the functionality and cellular architecture around a dental implant can be highly beneficial to our understanding of host–material–pathogen interactions in the context of peri-implant disease.

Here, we present the first dental implant-on-a-chip (IOC), a physiologically relevant *in vitro* model, for investigating host–material–pathogen interactions as a proof of concept. While cell-to-cell interactions in the context of various organ functions could be implemented in a typical organ-on-chip, integrating biomaterials into the microfluidic model can be technically challenging as the microchannels should provide sufficient space (especially height) to accommodate materials within the chip. Furthermore, two microchannels shall be separated by a porous membrane with small, closely spaced yet tall pores to culture distinct cell types. To overcome this hurdle, we adapted our previously reported backside UV lithography[20] to enable unprecedented high-aspect-ratio microchannels separated by closely spaced, tall, elliptical micropillars (replacing a porous membrane). We also employed a modular strategy for the incorporation of dental materials (such as dental crown resin and titanium implant post), which can be used for other applications. Through this, we successfully fabricated high-aspect-ratio SU-8 layers and resultant PDMS microchannels that have one side wall enclosed by biomaterials such that human gingival keratinocyte and fibroblast (HGKs and HGFs, respectively) populations interface with their respective dental materials (crown for HGKs and titanium for HGFs), mimicking the entire dental implant microenvironment. We verified our design *via* modeling the fluid dynamics within the IOCs to demonstrate minimal mixing between cell culturing microchannels while allowing cross-talking, leading to conducive growth conditions for both cell populations. After optimizing cell culture conditions within the IOCs, we challenged the keratinocyte layer with an oral pathogen, *Streptococcus mutans*, to mimic a bacterial insult. Furthermore, we tested the efficacy of photobiomodulation (PBM) therapy using this IOC to demonstrate its applicability as a therapeutic testing platform. We observed that microbial insult severely damaged HGKs, while PBM therapy effectively protected HGKs, exhibiting a ~3.5-fold lower loss in HGK in comparison to controls without PBM treatment. Overall, our IOCs represent a physiologically relevant *in vitro* model of the cellular microenvironment for the investigation of host–material–pathogen interactions and a therapeutic testing platform.

Materials and methods

General procedure for preparing PDMS

Polydimethylsiloxane (PDMS – Sylgard® 184, Dow Silicones Corporation, Midland, MI, USA) was prepared by mixing 10 : 1 wt% of base : crosslinker. The uncured polymer was poured over the SU-8 master molds, degassed for 30 min, and cured on a hotplate at 70 °C for 3 h.

Computer-aided design

All designs for the microfluidic layers, the constituent parts (dental resin block and titanium block), the geometries for fluid dynamics simulations and the custom chip-holder for photobiomodulation experiments were made in Autodesk® AutoCAD 2019.

Fabrication of master molds for microfluidic layers and dental resin blocks

Two-by-two-inch chromium-coated photomasks (Telic Company, Santa Clarita, CA, USA) were drop-coated uniformly with 840 mg of SU-82025 (Kayaku Advanced Materials, Inc., Westborough, MA, USA). The 840 mg weight indicated the master mold's thickness to be 210 μm after the soft baking process. This thickness of SU-8 was enough to ensure that the blocks remained rigid and could be handled without bending during chip assembly. The photomasks were then transferred to a conventional hotplate for a two-step soft-baking process: the hotplate was scheduled to heat up from 25 to 70 °C for 7 min and then from 70 to 95 °C for 40 min. After completing the soft-baking process and cooling the samples, they were exposed to broadband UV using a commercial UV exposure tool (Model 30 UV light source, Optical Associate Inc., Milpitas, CA, USA). For a total exposure time of 50 s, a constant UV intensity of 30 mW cm^{-2}

was applied. The samples were then returned to the hotplate for post-exposure bake (PEB) at temperatures ranging from 25 to 45 °C for 2 min, 45 to 65 °C for 3 min, and lastly 65 to 95 °C for 15 min. After completing the PEB and cooling the samples, they were immersed in SU-8 developer (Kayaku Advanced Materials, Inc.) for 10 min. Following that, samples were cleaned with isopropyl alcohol (IPA), dried using compressed air, and carefully stored for experimental use. The same procedure was utilized to create the master molds for the dental resin blocks, only a one-inch by one-inch photomask was employed.

Fabrication of dental resin blocks

PDMS was used as an intermediate in replica molding of the master molds for dental resin blocks (Fig. S1†). After curing, PDMS samples were peeled away and cleaned with scotch tape and IPA. Samples were then dried with compressed air. Precured, biocompatible Class IIa dental resin (C&B MFH, Next Dent B.V., Netherlands) was poured into slots within the PDMS molds. To obtain a uniform surface, a piece of UV transparency film (Apollo, ACCO Brands, Lake Zurich, IL) was gently placed onto uncured dental resin while releasing air bubbles. A UV LED flashlight with an irradiance of 4 mW cm^{-2} (V1 385–395 nm, uvBeast, Portland, OR, USA) was used to cure the dental resin blocks for 5 min. The transparency films were removed, and the blocks were rinsed with IPA and stored for experimental use. Resultant dental resin blocks were measured with a caliper with 0.01 mm resolution (Fowler, Canton, MA, USA) and found to be 230 ± 19 μm thick (Fig. S2†).

Fabrication of titanium blocks

The fabrication process was comparable to that for SU-8 master molds described previously with the following differences. 420 mg of SU-82025 was equally drop-coated onto one-inch by two-inch photomasks (Fig. S3†). After rinsing the samples with IPA to remove any remaining SU-8 developer, the samples were gently pressed to delaminate them from the photomask. The delaminated SU-8 samples were dried with compressed air and titanium metalized for 42 min at a deposition rate of 12 nm min^{-1} using a DC sputter (Korvus Technology, Maidenhead, UK) resulting in a final thickness of 500 nm. On the reverse side of the samples, the identical metallization procedure was performed. The metalized samples were then dried with compressed nitrogen and stored safely for experimental use. Resultant titanium blocks were measured with a caliper and found to be 217 ± 6 μm thick. (Fig. S2†).

Microfluidic chip assembly

Microfluidic layers of PDMS were fabricated from master molds using the general procedure described previously. Biopsy punches (1 mm diameter) were used to create inlets and outlets. PDMS microfluidic layers were cleaned with scotch tape and IPA, followed by a 15 min sonication in Milli-Q water (MilliporeSigma, Burlington, MA, USA). In parallel, glass slides were rinsed with IPA and sonicated with Milli-Q water. The constituent parts of the modular microfluidic chips – dental resin and titanium blocks, were then placed into slots within the microfluidic layers using the corners and curves of these blocks as alignment marks. A flat spatula was used to gently spread uncured PDMS onto the interface between the blocks and microfluidic layers that were farthest away from the cell culture chambers (to avoid clogging the channels and chambers of the microfluidic chip). These composites of microfluidic layers with embedded blocks were placed in an oven at 100 °C for 2 min to cure the PDMS coating. Finally, these composites were permanently bonded to glass slides using a plasma cleaner (PDC-32G, Harrick Plasma Inc., Ithaca, NY). Sealed chips were then sterilized under UV for 1 h and stored for experimental use.

Computational fluid dynamics

In order to predict and investigate flow characteristics in the microfluidic chip, the 2D finite element analysis (FEM) was performed with COMSOL Multiphysics software (V 6.0, COMSOL Inc., Burlington, MA). A physics-controlled mesh with extremely fine element size was created by the COMSOL built-in meshing method. All the physical properties of the water in the microfluidic chip were used directly from the COMSOL material library. The thickness of the microfluidic channel is 210 μm, the temperature is 37 °C, and the flow rate is 0.3 μL min^{-1} for each inlet. For rectangular microfluidic channels, shear stress can be derived as follows[21] when the length of the channel is much greater than the height and width:

$$\tau = \frac{6\mu Q}{h^2 w}$$

where τ is the shear stress, μ is the dynamic viscosity, Q is the flow rate, h is the height of the channel and w is the width of the channel. For each cellular chamber in the IOC, with h = 200 μm and w = 600 μm, the calculated shear stress was 0.009 dyn cm^{-2}.

The stationary study of the laminar flow module was conducted to simulate the incompressible steady-state flow profile in the microfluidic chip. The time-dependent study of transport of diluted species modules and previous stationary study solutions were used to account for the mass transfer between upper and lower channels. Inlet 1 was filled with a higher concentration (1 mol m^{-3}), while inlet 2 was filled with a lower concentration (0 mol m^{-3}). For the concentration of diluted species, 1 mol m^{-3} at inlet 1 and 0 mol m^{-3} at inlet 2 were applied. The simulations accounting for the limited transport of sub-micron-sized bacteria from the upper channel to the lower channel in the presence of a flow were conducted using the particle tracing module and previous stationary study solutions. A 0.5 μm particle diameter and a 1100 kg m^{-3} particle density were used to mimic bacterial cells. The sub-micron-sized particles were uniformly released over

a 2500 s period at inlet 1, 100 particles at a time, with a total number of particles of 100 000.

Experimental validation of small particle transport

To experimentally validate the minimal mixing nature of small particles flowing through the IOC, we conducted a time-series experiment with GFP-labeled *S. mutans* UA159. Briefly, a bacteria-laden solution (~10^6 CFU mL^{-1} in PBS) was flowed through the upper chamber (meant for keratinocytes) at 0.3 μL min^{-1}. Simultaneously, bacteria-free PBS was flowed through the lower chamber (meant for fibroblasts) at 0.3 μL min^{-1}. Snapshots of the central part of the IOC were taken at 0, 1, 2, and 4 h with a Leica DMi8 (Leica Microsystems, Deerfield, IL, USA).

Cell culture in chip and continuous flow experiments

HGKs (kindly provided by the laboratory of Dr. Dana T. Graves, School of Dental Medicine, University of Pennsylvania) and HGFs (kindly provided by the laboratory of Dr. Jonathan Korostoff, School of Dental Medicine, University of Pennsylvania) were used for all experiments. Cells were maintained in their respective culture media (HGKs: keratinocyte basal medium (KBM-Gold, Lonza Group AG, Basel, Switzerland) supplemented with the KGM-2 SingleQuots kit (Lonza); HGFs: fibroblast basal medium (ATCC, Manassas, VA, USA) supplemented with the fibroblast growth kit (ATCC, PCS-201-041) and 1% v/v Anti–Anti (Gibco, Gaithersburg, MD, USA)) and incubated at 37 °C in a humidified atmosphere of 5% CO_2 until confluence. Before seeding chips with cells, 50 μg mL^{-1} of collagen type I (Sigma-Aldrich, St. Loius, MO, USA) was flowed through the chips at 0.3 μL min^{-1} for 1 h (dual NE-4000 syringe pumps, New Era Pump Systems Inc., Farmingdale, NY, USA) to coat the glass slides and make them conducive substrates for HGK and HGF attachment. 10 000 cells per mL of each cell type were then flowed into their respective chambers at 0.3 μL min^{-1} and the flow was stopped for 4 h to allow initial adhesion of cells to the collagen-coated glass slides. After initial adhesion was confirmed, the flow of respective media was maintained in the chambers for 3 days at 0.3 μL min^{-1} until both populations of cell types were confluent in their respective chambers.

Fabrication of the PBM platform

To mimic PBM therapy in the microfluidic chip, a custom chip holder was designed and 3D printed (Form 2, FormLabs, Somerville, MA, USA). Our custom chip-holder was a miniaturized form of a LED platform that we have previously optimized for use in host–pathogen investigations.[22] Briefly, red LEDs (λ = 615 nm; SML-P12U2TT86R, ROHM Semiconductor, UK) were used on a miniaturized LED platform that was fabricated by connecting a resistor in series with an LED (1.2 kΩ) to limit the current and protect the electronics. Irradiance was kept consistent with our previous study[22] by using the irradiation profile in Fig. S4.† After the LED circuit was assembled on a printed circuit board, it was placed in a slot of a 3D printed block, followed by electrical and thermal passivation by 3D printing resin. Using insulated wires (29 AWG), the LED circuit was connected to a power supply as described previously.[22]

Bacterial challenge and photobiomodulation experiments

S. mutans UA159, a cariogenic oral pathogen, was used for bacterial challenge experiments. Stocks were stored at −80 °C in tryptic soy broth containing 50% glycerol. Strains were grown to the mid-exponential phase in ultrafiltered (10 kDa molecular-mass cutoff; Millipore, Billerica, MA, USA) tryptone–yeast extract broth (UFTYE; pH 7.0) containing 1% glucose.[23,24] Cells were harvested by centrifugation (5500*g*, 10 min, 4 °C). *S. mutans* UA159 was transferred from the stock culture to the culture medium (UFTYE containing 1% glucose) and incubated overnight at 37 °C and 5% CO_2. From this culture, bacteria were transferred onto a fresh culture medium and incubated at 37 °C and 5% CO_2 to mid-exponential phase (optical density of 1.0 at 600 nm corresponding to 2 × 10^9 CFU mL^{-1}). After confluency was attained for both cells on day 3, the chips were placed in custom chip holders and subjected to LED treatment for 90 minutes. Control chips were placed in the chip holders but not subjected to LED treatment. An optimized density of 7 × 10^6 CFU mL^{-1} of *S. mutans* was added to antibiotic-free KBM-Gold cell culture media and bacteria-laden media was flowed through the HGK chamber for 24 h. Images of 3 random areas (representing 50% of the width of the cell chambers) of cells in both chambers were taken at 0 and 24 h (representing before and after bacterial challenge). To assess the growth of *S. mutans* in the input media, the number of viable bacterial cells (CFU mL^{-1}) in the input reservoir was determined at 0 and 24 h by taking out 400 μL of the reservoir at these time points and plating it on blood agar plates (BD BBL prepared plated media : trypticase soy agar (TSA II) with sheep blood, Thermo Fisher Scientific, Waltham, MA, USA). All experiments were conducted 3 times resulting in a total of 9 before–after image pairs and 6 CFU mL^{-1} counts per condition.

Staining, imaging, and quantification

Cultured HGKs and HGFs were fixed using 4% paraformaldehyde solution (Santa Cruz Biotechnology, Inc., Dallas, TX, USA) for 15 min at 37 °C and then rinsed with PBS three times for 5 minutes each. Once fixed, cells were permeabilized with 0.1% Triton X-100 (Sigma-Aldrich) in PBS for 10 min at room temperature, followed by three 5 min rinses with PBS. Cells were then stained with Dylight™ 650 phalloidin (Cell Signaling Technology, Danvers, MA, USA; Ex/Em: 651/672 nm) diluted 1 : 20 in PBS for 15 minutes at room temperature in the dark and then rinsed once with PBS. Finally, cells were stained with DAPI (Invitrogen, Waltham, MA, USA; Ex/Em: 358/461 nm) using 1 μg ml^{-1} of PBS for 5 minutes at room temperature in the dark and then rinsed

once with PBS. Immediately after completion of staining, cells were imaged using a confocal microscope (LSM800, Zeiss, Jena, Germany) at 10× magnification.

Master molds for microfluidic layers and titanium blocks were imaged using a digital microscope (Smartzoom 5, Zeiss, Jena, Germany). SEM images were taken with a PS-210 (PEMTRON Co. Ltd., Seoul, South Korea). Top view images of PDMS microfluidic layers were taken with a Zeiss Axiovision microscope (Zeiss). Cell culture images were taken with a Nikon TMS inverted phase-contrast microscope (Nikon Inc., Melville, NY, USA) fitted with a camera at 10× magnification. The surface area coverage, raw cell number, and cell size for each image were estimated using ImageJ (Fiji[25]) and its cell counter plugin, respectively. The surface coverage was compared between the IOC and culture flasks, and between different regions within the IOC, using ImageJ. By normalizing values to those from 0 h images, the percentage drop in surface area coverage and percentage drop in cell number were estimated.

Statistical analysis

All experiments were conducted at least three times with all data represented as mean ± SD. GraphPad Prism was used for all statistical analyses. Significant differences in data were assessed using unpaired *t*-tests with a significance level set to $p < 0.05$.

Results

IOC design and assembly

A typical organ-on-a-chip allows culturing of distinct cell types in the top and bottom microchannels that are separated by a porous membrane (as a representative of the cell membrane). Embedding biomaterials into a microfluidic device, especially to interface with cells, requires significant modification to the overall design, including microchannel orientation, dimension, and cell membrane-mimicking porous membrane. The IOC is designed to mimic the microenvironment in the vicinity of a dental implant (Fig. 1A–C). As illustrated, two representative dental implant components, *i.e.*, dental resin and titanium, are faced with two types of gingival soft tissues, HGKs (Fig. 1D) and HGFs (Fig. 1E).

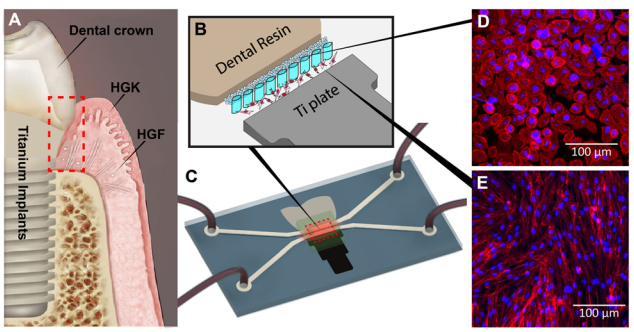

Fig. 1 Implant-on-a-chip (IOC) for *in vitro* modeling of interactions between peri-implant soft tissues and implant components. (A) Illustration of dental implants and nearby soft tissues. (B) Schematic design of IOC, mimicking the dental implant microenvironment. (C) Close-up view of microfluidic channels separated by elliptical micropillars; dental resin and the titanium plate are integrated into the IOC while facing human gingival keratinocytes (HGKs) and fibroblasts (HGFs), respectively. Representative confocal images of (D) HGKs and (E) HGFs, displaying high confluence. Blue: cell nuclei stained with DAPI; red: actin filaments stained with phalloidin.

As the dental IOC structure is PDMS-converted from the SU-8 master mold, the SU-8 lithography performance is highly reliant on process parameters to achieve high-resolution, stable microstructures,[26] which must be fine-tuned to get optimal results. The overall height was designed to be >200 μm mainly to seamlessly accommodate the dental materials, and the microchannel width was set to 600 μm. To integrate biomaterials in a modular manner, the cell culturing space (middle of the IOC) was designed to be large void spaces, which were later inserted with the material and formed seamless microchannels aligned with the inlet and outlet. Fig. 2A–F illustrate the fabrication process of the master mold for the IOC. To prepare the mold, CAD of the photomask (Fig. 2G) was prepared and chromium-coated photomasks were drop-coated uniformly with SU-82025, followed by a two-step soft-baking process. This resulted in the master mold's thickness being ~210 μm. Then, the mold was exposed to broadband UV for 50 s at a constant intensity of 30 mW cm^{-2}. After completing the three-step post-exposure bake and immersing in SU-8 developer for 10 min, the master mold was prepared. The SEM images of the SU-8 microstructures showed the separation between the elliptical microtrenches (Fig. 2H) and the top and side views of a SU-8 mold on glass depicted the achieved average wall size and SU-8 thickness (Fig. 2I).

A similar procedure was utilized to create the master molds for the dental resin and titanium blocks. ESI† Fig. S1 and S3 illustrate the overall process of fabricating the dental resin and titanium blocks. The tooth-shaped dental crown material is fabricated from commercial crown resin (Fig. S1†). Similarly, the titanium implant post is shaped like a screw (Fig. S3†). Apart from the aesthetic resemblance to a dental implant, the primary purpose of the curvatures in the dental resin and titanium blocks was to serve as alignment marks during the IOC assembly. The microfluidic layers of PDMS were fabricated from master molds, and biopsy punches (1 mm diameter) were used to create inlets and outlets. Fig. 3A–G illustrate the assembly of the IOC. After cleaning, the prepared dental resin and titanium blocks were placed into slots within the microfluidic layers. Uncured PDMS was spread onto the interface between the blocks and microfluidic layers to create tight sealing. The composite of the microfluidic layer with embedded blocks was placed in an oven to cure the PDMS coating; in turn, the composite was permanently bonded to glass slides using a plasma cleaner. Fig. 3H–N show the images of a PDMS microfluidic layer, depicting 14 elliptical micropillars separated by 10 μm pores to segregate channels for distinct cell types. A picture of the PDMS microfluidic layer without dental resin and titanium blocks is shown in Fig. 3O, and the composite

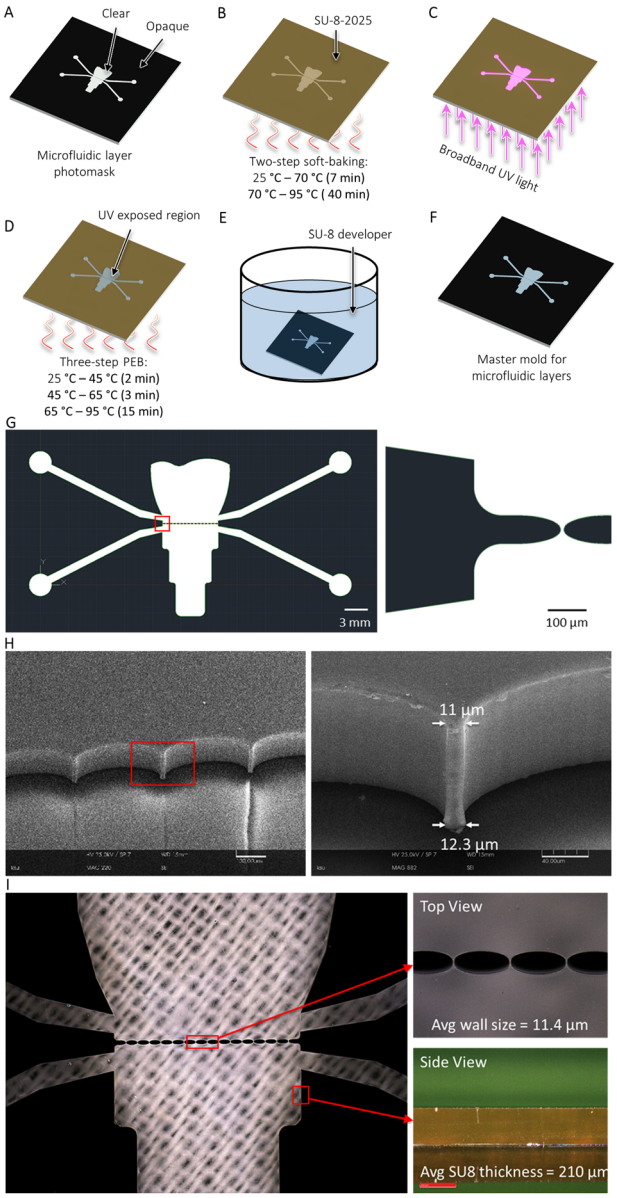

Fig. 2 Schematic diagram for master mold fabrication and the SU-8 master mold used to form microfluidic layers. (A) Chromium-coated photomask. (B) Soft-baking process. (C) Exposure to broadband UV. (D) Post-exposure baking process. (E) Immersion into SU-8 developer. (F) Final SU-8 master mold. (G) CAD of the photomask. Inset: Zoomed-in version of the elliptical microstructures. (H) SEM image of the SU-8 microstructures. Inset: Zoomed-in image of the separation between the elliptical microtrenches. (I) Top view of an SU-8 master mold. Insets: Zoomed-in top and side views depicting the average wall size and SU-8 thickness.

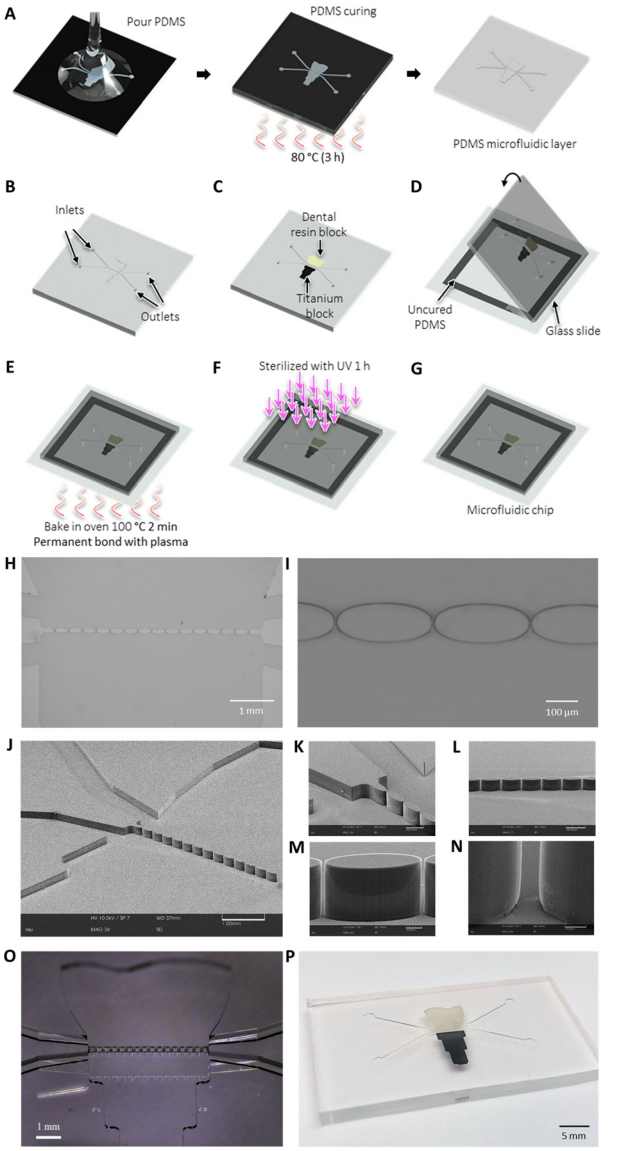

Fig. 3 Assembly of the implant-on-a-chip (IOC) and components for the modular assembly of the IOC. (A) Addition of uncured PDMS to the master mold followed by curing and release of the PDMS microfluidic layer. (B) Creation of inlets and outlets. (C) Embedment of dental resin and titanium blocks with a coating of PDMS. (D) Curing of the PDMS coating and (E) plasma bonding of the PDMS layer to glass. (F) Sterilization of the IOC. (G) Assembled IOC ready for experimental use. (H) Image of a PDMS microfluidic layer depicting 14 elliptical micropillars separated by 10 µm pores. (I) Zoomed-in image of the pores. (J) SEM image of the PDMS microfluidic layer with (K) zoomed-in versions and (L)–(N) depicting sequentially larger magnifications of side-on views. (O) Image of the PDMS microfluidic layer without dental resin and titanium blocks. (P) Composite microfluidic layer with PDMS and blocks.

microfluidic layer with PDMS and blocks is shown in Fig. 3P. The IOC was ready for use in proof-of-concept host–material–pathogen investigations.

Optimization of cell culture

The ability to cultivate two unique cell types in a microfluidic chip without physical mixing while permitting cross-talk is the key to mimicking host–pathogen interactions *in vitro*. An important benefit of conducting experiments in microfluidic settings is the predictable behavior of the fluid dynamics with laminar flow.[2] Given that the IOC should generate spatially separated cell populations of HGKs (in the upper chamber for top view) and HGFs (in the lower chamber for

top view), it was imperative to study fluid dynamics within the IOC prior to biological testing. Thus, we ran computational fluid dynamics (CFD) simulations (COMSOL Multiphysics®, COMSOL; see Materials and methods for details) in the microchamber (Fig. 4A). Additionally, it was important to ensure that we used an optimal flow rate during the experiments. Based on the limited existing literature available from microfluidic models (involving keratinocytes[27] and fibroblasts[28]), we established an optimal flow rate of 0.3 μL min^{-1} for cell experiments in the IOC. It is well-known that keratinocytes are extremely mechanoresponsive and start showing morphological variation and cytoskeletal reorganization with as little as 0.06 dyn cm^{-2}.[29] Thus, our intention was to minimize all morphological variations induced by the flow of nutrient media and focus on co-culturing cells with implant materials under dynamic settings. The resultant shear stress in the microfluidic channels was 0.009 dyn cm^{-2}. Overall, our microchamber design with 10 μm pore microtrenches exhibited highly suitable laminar flow paths with minimal mixing at a flow rate of 0.3 μL min^{-1}. We also simulated the effect of the specimen size with two different sizes of molecules/particles (Fig. 4B–D). By flowing small molecules through inlet 1, using a diffusion coefficient of glucose in water at 37 °C (9.59 × 10^{-10} m^2 s^{-1}),[30] we observed that the molecules started to mix as soon as they entered the microchamber, which continued toward the outlets over time (Fig. 4B and D). In contrast, when particles with 0.5 μm diameter were released from inlet 1, they did not appear in outlet 2, indicating no significant mix regardless of spatial or temporal stimulation (Fig. 4C and D). In other words, the simulation results clearly prove that the pore width (10 μm) chosen for the IOC chip can resemble the cell membrane function (allowing each cell to access their respective nutrient media without chaotic mixing while serving as a protective barrier for underneath tissues from other organisms such as bacteria), suitable for the subsequent biological experiments. To experimentally validate the minimal mixing nature of the IOC with small particles, a bacteria-laden solution (GFP *S. mutans*) was flowed through the upper chamber (meant for keratinocytes) while a bacteria-free solution was flowed through the lower chamber (meant for fibroblasts) at 0.3 μL min^{-1}. As clearly demonstrated in Fig. S5,† bacterial cells predominantly remained within the chamber through which they were introduced (keratinocyte chamber), while there was minimal mixing of these particles into the fibroblast chamber. This information along with Fig. 4F and G distinctly proves that the porous membrane in our IOC can be used to avoid mixing of the solutions in the two chambers, allowing us to have spatially separate co-cultures of different cell types (similar to human physiology) and selectively challenge the epithelial cells in our model with relevant bacteria.

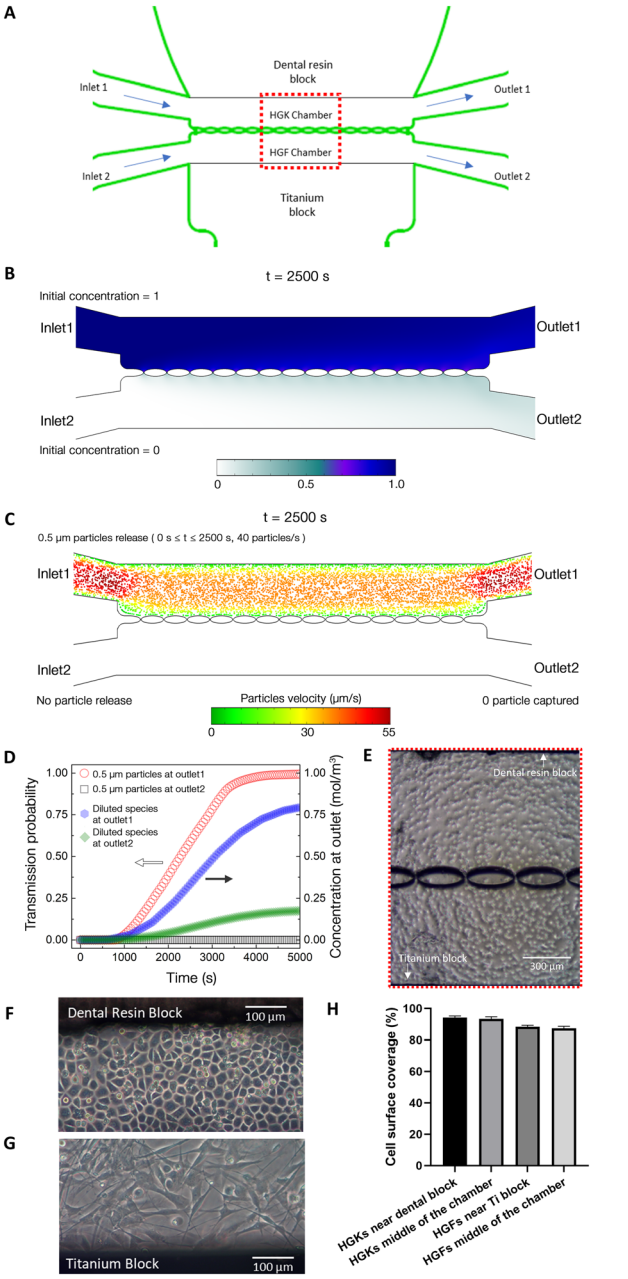

Fig. 4 Cell culture within IOCs. (A) Schematic of the fluidic environment of the IOC with separate chambers for HGKs and HGFs. (B) Simulation of small molecules flowing in *via* inlet 1. (C) Simulation of 0.5 μm particles entering *via* inlet 1. (D) Concentration at the outlet and transmission probability *vs.* time. (E) 4× image of HGKs and HGFs after seeding demonstrating a homogeneous distribution of spatially separated cell populations. (F) Representative 10× image of HGKs in their chamber and their interface with dental resin blocks. (G) Representative 10× image of HGFs in their chamber and their interface with titanium blocks. (H) Comparison of cell surface coverage at different locations within the chambers.

The CFD simulation was verified by culturing HGKs and HGFs within the chips for continuous flow experiments. We cultured both HGKs and HGFs in their respective chambers while interfacing with models of dental crowns (dental resin blocks) and titanium posts (titanium blocks). As shown, an input flow rate of 0.3 μL min^{-1} and cell seeding density of 10 000 cells per mL ensured a homogeneous distribution of spatially separated cell populations in their respective chambers on day 0 (Fig. 4E). Over the next 3 days, HGKs

formed close cell–cell contacts to form a monolayer of confluent epithelial cells in the proximity of the dental resin block (Fig. 4F). Similarly, HGF chambers interfacing with the titanium block were confluent with elongated morphology by day 3 (Fig. 4G). Excitingly, we found that there were no significant differences in cell densities between the IOC and a traditional cell culture flask (Fig. S6†). Furthermore, quantified local cell densities nearby dental blocks and the middle of each chamber revealed that the dental resin and titanium blocks did not compromise the colonization of HGKs and HGFs, respectively (Fig. 4H). In fact, both cell types were seen to be in direct contact with and conform to their respective material from top-down images (Fig. S7†). These are strong indicators that both cell populations adjusted well to their environment in the IOC. Our results represent the first demonstration of interfacing hard dental materials of an implant with epithelial and connective tissue cells in a microfluidic setting. These results established our model as a suitable platform for conducting host–pathogen investigations in physiologically relevant settings.

Bacterial challenge and photobiomodulation

Once our cell culture conditions were optimized, we performed proof-of-concept bacterial challenge experiments and tested the protective ability of PBM therapy within our system. In our previous study, we investigated the effects of blue, green, red, and near-infrared light on HGK numbers that were infected with lipopolysaccharides.[22] We observed that red or near-infrared light significantly increased cell numbers relative to non-irradiated controls.[22,31] In contrast, green light did not affect cell proliferation, whereas blue light caused extensive photocytotoxicity.[22] To corroborate our previous findings of the protective effect of PBM therapy on keratinocytes and to demonstrate the amenability of our system with PBM-based investigations, we utilized red light and tested chips under two conditions – with and without LED treatment before the bacterial challenge. For LED treatment, the chips were placed in custom chip-holders designed for near-contact PBM therapy (Fig. 5A and B).

To mimic bacterial challenge in the oral cavity, *Streptococcus mutans* was added to an antibiotic-free HGK nutrient medium, and this medium was used to challenge the HGK layer for 24 h. By testing various densities of *S. mutans*, we found that flowing lower than ~1×10^6 CFU mL^{-1} of *S. mutans* at a flow rate of 0.3 μL min^{-1} did not cause severe damage to HGKs (Fig. S8†). Seeding densities of ~7×10^6 CFU mL^{-1} of *S. mutans* induced severe loss of HGKs, thus it was chosen for the bacterial challenge experiment. Higher seeding densities of ~2×10^7 CFU mL^{-1} produced an extremely high loss of cell coverage (Fig. S8†) and were disregarded for bacterial challenge experiments. Representative images at 0 and 24 h demonstrated that HGK monolayers appeared to be less confluent and showed limited cell–cell contact when cultured with *S. mutans* without PBM treatment (Fig. 5C and D) while there was an

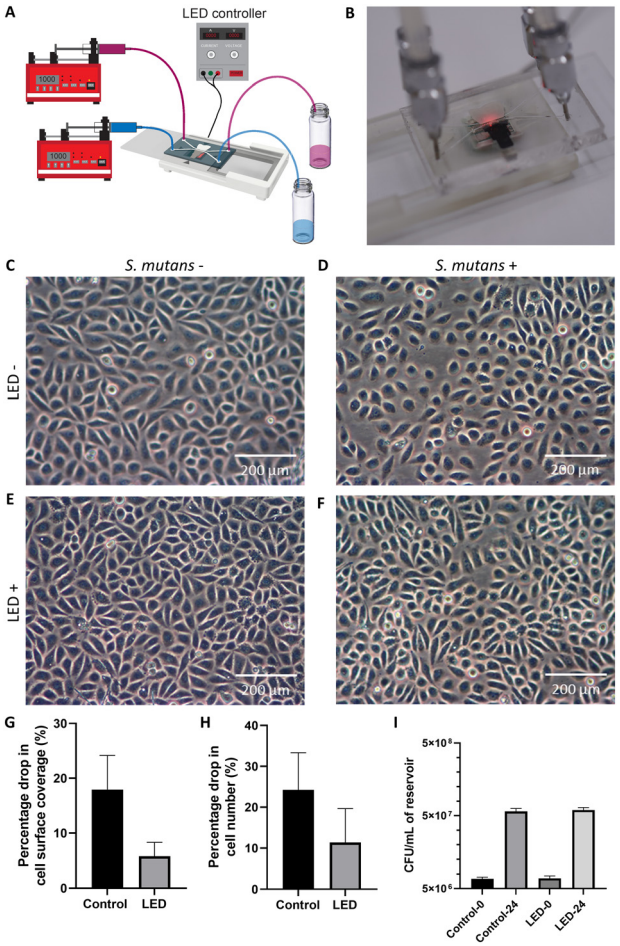

Fig. 5 Bacterial challenge to HGK layers and PBM therapy. (A) Schematic of a flow experiment in the IOC in conjunction with PBM therapy. (B) Close-up view of the IOC during a bacterial challenge experiment with PBM therapy. *S. mutans* was used to challenge the HGK layers of control and LED-treated chips. Representative images of HGKs in control chips at (C) 0 h and (D) 24 h. Representative images of HGKs in LED-treated chips at (E) 0 h and (F) 24 h. Percentage drop after 24 h in (G) cell surface coverage and (H) cell number for control and LED-treated chips. (I) CFU mL^{-1} of the input reservoir at 0 and 24 h for control and LED-treated chips * represents *t*-tests with $p < 0.05$; ($n > 3$).

insignificant increase in the average cell size for keratinocytes (~0.1%) (Fig. S9†). In contrast, PBM-treated HGKs already showed increased confluence before microbial challenge and exhibited minimal damage against *S. mutans* infection for 24 h (Fig. 5E and F). A set of 9 before–after image pairs per condition were used for quantification of the percentage drop in cell surface coverage (Fig. 5G) and cell number (Fig. 5H). Overall, loss of cell surface coverage was 3.5-fold greater in control chips in comparison to LED-treated chips. This was a direct consequence of a significant number of cells being detached in the control chips due to bacterial insult for 24 h. Accordingly, there was a 2.5-fold greater drop in cell number for control chips in comparison to LED-treated chips. To confirm that there was bacterial growth during the challenge, we quantified the CFU mL^{-1} of *S. mutans* in the input

reservoir at 0 and 24 h. Under both control and LED-treated conditions, there was a 1 log increase in CFU mL^{-1} and visible turbidity in the reservoir after 24 h, indicating that light irradiation can boost HGKs in resisting recurrent bacterial challenges up to $\sim 5 \times 10^7$ CFU ml^{-1} of pathogens (Fig. 5I). Our results indicated that LED treatment was beneficial for the HGK layer.

As further proof of the laminar nature of the fluid dynamics of our system, we also imaged the HGF layer at 0 and 24 h post bacterial challenge to the HGK layer (Fig. S10†). Encouragingly, we noticed no significant damage to the HGF layer after bacterial challenge in either of the chips (control or LED-treated). This validated the minimal mixing between the spatially separated cell populations within the IOC as well as the unique characteristics of keratinocytes as a protective barrier against bacterial challenges. Overall, our results highlight the IOC as a novel, modular, microfluidic platform to conduct physiologically relevant host–pathogen interactions and assess the feasibility of strategies such as PBM therapy.

Discussion

Microfluidic physiological systems have garnered tremendous interest in recent years because of their usefulness in providing novel insights into normal human function and their potential to be informative for the discovery and development of therapeutic strategies.[32–34] Although animal models have been useful in improving our understanding of the physiology and pathogenesis of diseases, these models are generally expensive and time-consuming but poorly predict human physiology, particularly for drug development.[35] As such, there has been a constant and undeniable need for models that more accurately predict human responses.[36] However, due to ethical concerns and the limitation of invasive procedures, collecting tissue samples from human subjects is often extremely difficult or impossible. Notably, microfluidic technologies offer a powerful screening platform for healthcare monitoring and therapeutics by replicating *in vivo* conditions with the low-cost and rapid fabrication of the chip.[37–39] With significant advances in microfabrication, dynamic *in vitro* systems are increasingly gaining traction as relevant models of tissue microenvironments.

Such microfluidic models can be highly beneficial for dental research because the oral cavity is a representative part of the human body that harbors a diverse array of organisms, including microbes and soft/hard tissues, and microfluidic models can enable precise spatiotemporal assessments of those interactions.[40] Recently, another component, biomaterials in a denture or implant, was added into those interactions, which serve an essential role in local and systemic health. However, microfluidic models have been employed infrequently in dental research so far. While some studies introduced microfluidics to investigate the oral environment, these studies focused on either the oral mucosa or the dentin–pulp interface.[27,41–44] For example, França *et al.* developed and validated a tooth-on-a-chip platform to replicate the pulp–dentin interface and study the dental pulp cell response to biomaterials.[42] Subsequently, Rodrigues *et al.* used the tooth-on-a-chip platform to model the biomaterial–biofilm–dentin interface using *S. mutans* to test the antimicrobial efficacy of calcium silicate cement.[44] Similarly, as a proof-of-concept, *S. mutans* has been used to test bacterial invasion on keratinocytes in an oral mucosa-on-a-chip model.[43] Importantly, none of these studies represent models of host–material–pathogen interactions for dental implants. With modular microfluidics becoming increasingly prevalent, studying these interactions around dental implants using microfluidics is a logical progression and can significantly improve our biological understanding of the oral environment.

The osseointegrated implant is one of the important areas for human health where material–cellular interactions play critical roles. In the oral environment, the tissue that surrounds a tooth/implant is composed of epithelial cells and connective tissue. Unlike tight seals around natural teeth in a healthy individual, incomplete tissue sealing around an implant leaves it more vulnerable to bacterial infiltration and subsequent cellular inflammation.[45] Such peri-implant diseases could lead to destructive failures, resulting in discomfort, painful and costly surgical replacement of failed implants, and the potential breakdown of the overall oral health.[46–48] This provides a strong justification for investigations of host–material–pathogen interactions that improve our understanding of the biology involved. Although dental implant surface properties play important roles in the inflammatory response of the adjacent peri-implant mucosal tissue, this has not been explored using microfluidic models yet.

Here, we have developed the first instance of a microfluidic implant on a chip system. In order to mimic the cellular environment around a dental implant, it is important to establish epithelial (HGKs) and connective tissue (HGFs) layers that interface with dental materials. However, developing a microfluidic environment with dental materials adds complexities to the fabrication strategy and protocol. Typically, microfluidic chips for biological experiments are required to have much wider microchannel dimensions for reliable large population cell culture than those for chemical assays.[49,50] Furthermore, it is critical to have sufficient channel height to incorporate biomaterials (with hundreds of micrometers in thickness) into microfluidic chips. Although large channel width dimensions can be easily achieved (often up to 1 mm wide), it is extremely challenging to increase the height of the channel while maintaining a porous membrane between two channels; maintaining cell separation in chips necessitates the inclusion of a tall porous barrier with closely spaced pores in co-culture environments, however, traditional photolithographic techniques are not amenable to generating closely-spaced tall features due to the limited height-to-width aspect ratio (5 : 1).[51]

To overcome this technical challenge, we applied our previously developed backside UV exposure schemes with a

selective optical filter[20] to allow the generation of closely-spaced microtrenches in SU-8 master molds (practical height-to-width aspect ratio of 25), and developed modular microfluidic chips with biomaterials. We kept PDMS as the material for our microfluidic layers because of its optical clarity, biocompatibility, flexibility, and amenability for use in high-fidelity replica molding.[52] The molds and microfluidic layers developed using this scheme as well as the assembled microfluidic device with seamlessly incorporated biomaterials are shown in Fig. 2 and 3. As reported, microfluidic systems almost always operate in the laminar flow regime leading to predictable fluid dynamics.[2] Our simulations (Fig. 4) also predicted laminar fluid streams with minimal mixing between cell chambers while allowing cross-talk between two channels to help maintain ideal culture conditions for both HGKs and HGFs in their respective nutrient media. At a flow rate of 0.3 μL min^{-1}, we generated spatially separated confluent populations of HGKs and HGFs (Fig. 4). Altogether, the data revealed that we successfully created spatially separated cell populations that interface with their respective dental material (crown for HGKs and titanium for HGFs) in a new conceptual microfluidic chip.

Another advantage of using a microfluidic approach is the transparency of the materials used in fabrication (most commonly, PDMS and glass). Apart from the usefulness in imaging, this transparency also makes microfluidic devices amenable for use with photobiomodulation (PBM) therapy. PBM therapy has been shown to promote tissue healing and reduce cellular inflammation.[53,54] In particular, studies have shown that red-to-infrared wavelengths enhance cell proliferation and prevent inflammation of human keratinocytes.[55,56] In fact, we have previously evaluated near-contact PBM therapy on keratinocytes *in vitro* and investigated its efficacy on host–pathogen interactions.[22] Additionally, we have developed a smart dental implant system for PBM therapy on gingival keratinocytes.[31] Thus, the IOC model combined with the PBM therapy module can be a useful tool to test the efficacy of PBM therapy in preventing implant infection and serves as a logical extension of our previous work. Here, we demonstrated the usefulness of PBM therapy in protecting epithelial cells from bacterial invasion (by *S. mutans*) and subsequent damage (Fig. 5). Furthermore, the laminar nature of the fluid dynamics in our model prevented the HGF layers from any significant damage by *S. mutans* (Fig. S10†).

Conclusions

In summary, the IOC features potential versatility for various research purposes. Given the microfluidic nature of our model, it is feasible to design multiplexed experimental strategies that can test epithelial invasion by several different pathogens as single species and multispecies. Our proof-of-concept study sets the stage for studying complex, multispecies biofilm formation under clinically relevant settings and testing PBM strategies in such environments. It is also possible to test the effect of exposing the cell-hard tissue interface in implants to different dental monomers. Additionally, to model hypoxic microenvironments, it is possible to decrease the local oxygen concentration in the HGK layer. Furthermore, the PBM amenability of our system can be expanded to incorporate testing of several configurations of LEDs in pulsed or continuous mode. Lastly, our modular fabrication strategy can be extended beyond dentistry to counter the effect of microbe-mediated inflammation on implantable devices placed in extraoral soft and/or hard tissues such as prosthetic joints and limbs. Overall, we present the first, physiologically relevant *in vitro* model of the microenvironment around dental implants for investigation of host–material–pathogen interactions and testing PBM strategies.

Author contributions

Atul Dhall: methodology, investigation, formal analysis, data curation, writing – original draft, writing – review & editing, visualization. Jun Ying Tan: methodology, investigation. Min Jun Oh: software, formal analysis, investigation. Sayemul Islam: investigation, visualization. Jungkwun Kim: conceptualization, methodology, writing – review & editing, supervision, project administration, funding acquisition. Albert Kim: conceptualization, methodology, writing – review & editing, supervision, project administration, funding acquisition. investigation. Geelsu Hwang: conceptualization, methodology, writing – review & editing, supervision, project administration, funding acquisition.

Conflicts of interest

There are no conflicts to declare.

Acknowledgements

We would like to thank Dr. Korostoff and Dr. Graves at the School of Dental Medicine, University of Pennsylvania for providing HGF and HGK cells, respectively. This work was financially supported by the National Institutes of Health, National Institute of Dental and Craniofacial Research grant DE027970 and National Science Foundation grant ECCS-2225697 (GH), National Science Foundation grant ECCS-2300985, ECCS-2306330, and ECCS-2245092 (AK), and National Science Foundation grant ECCS-2029086 and ECCS-2054567 (JK). Minjun Oh is a recipient of the Basic Science Research Program through the National Research Foundation of Korea funded by the Ministry of Education (NRF-2021R1A6A3A03044553).

References

1 Y. Yang, Y. Chen, H. Tang, N. Zong and X. Jiang, *Small Methods*, 2020, **4**, 1900451.

2 E. K. Sackmann, A. L. Fulton and D. J. Beebe, *Nature*, 2014, **507**, 181–189.
3 B. Zhang, A. Korolj, B. F. L. Lai and M. Radisic, *Nat. Rev. Mater.*, 2018, **3**, 257–278.
4 K. Duval, H. Grover, L.-H. Han, Y. Mou, A. F. Pegoraro, J. Fredberg and Z. Chen, *Physiology*, 2017, **32**, 266–277.
5 H. J. Kim, D. Huh, G. Hamilton and D. E. Ingber, *Lab Chip*, 2012, **12**, 2165–2174.
6 J.-M. Prot, A. Bunescu, B. Elena-Herrmann, C. Aninat, L. C. Snouber, L. Griscom, F. Razan, F. Y. Bois, C. Legallais and C. Brochot, *Toxicol. Appl. Pharmacol.*, 2012, **259**, 270–280.
7 D. Huh, D. C. Leslie, B. D. Matthews, J. P. Fraser, S. Jurek, G. A. Hamilton, K. S. Thorneloe, M. A. McAlexander and D. E. Ingber, *Sci. Transl. Med.*, 2012, **4**, 159ra147.
8 Y.-S. Torisawa, C. S. Spina, T. Mammoto, A. Mammoto, J. C. Weaver, T. Tat, J. J. Collins and D. E. Ingber, *Nat. Methods*, 2014, **11**, 663–669.
9 J. Seo, W. Y. Byun, A. Frank, M. Massaro-Giordano, V. Lee, V. Y. Bunya and D. Huh, *Invest. Ophthalmol. Visual Sci.*, 2016, **57**, 3872.
10 A. Guan, Y. Wang, K. S. Phillips and Z. Li, *Lab Chip*, 2016, **16**, 1152–1156.
11 F. Sharifi, S. S. Htwe, M. Righi, H. Liu, A. Pietralunga, O. Yesil-Celiktas, S. Maharjan, B. H. Cha, S. R. Shin and M. R. Dokmeci, *Adv. Healthcare Mater.*, 2019, **8**, 1801425.
12 J. Tillander, K. Hagberg, L. Hagberg and R. Brånemark, *Clin. Orthop. Relat. Res.*, 2010, **468**, 2781–2788.
13 B. Klinge, M. Hultin and T. Berglundh, *Dent. Clin. North Am.*, 2005, **49**, 661–676.
14 J. S. Dhaliwal, N. A. Abd Rahman, L. C. Ming, S. K. S. Dhaliwal, J. Knights and R. F. Albuquerque Junior, *Front. Cell. Infect. Microbiol.*, 2021, 922.
15 P. Sahrmann, F. Gilli, D. B. Wiedemeier, T. Attin, P. R. Schmidlin and L. Karygianni, *Microorganisms*, 2020, **8**, 661.
16 H. Elani, J. Starr, J. Da Silva and G. Gallucci, *J. Dent. Res.*, 2018, **97**, 1424–1430.
17 S. R. Dutta, D. Passi, P. Singh, M. Atri, S. Mohan and A. Sharma, *Natl. J. Maxillofac. Surg.*, 2020, **11**, 14.
18 A. Hanif, S. Qureshi, Z. Sheikh and H. Rashid, *Eur. J. Dent.*, 2017, **11**, 135–140.
19 R. Pokrowiecki, A. Mielczarek, T. Zaręba and S. Tyski, *Ther. Clin. Risk Manage.*, 2017, **13**, 1529.
20 J. J. Kim, H. Al Thuwaini and M. Almuslem, *Micro Nano Syst. Lett.*, 2018, **6**, 1–9.
21 F. Pisapia, W. Balachandran and M. Rasekh, *Appl. Sci.*, 2022, **12**, 3829.
22 H. E. Kim, S. Islam, M. Park, A. Kim and G. Hwang, *Adv. Biosyst.*, 2020, **4**, 1900227.
23 H. Kim, A. Dhall, Y. Liu, M. Bawazir, H. Koo and G. Hwang, *mBio*, 2021, **12**, e00651-21.
24 A. Dhall, S. Islam, M. Park, Y. Zhang, A. Kim and G. Hwang, *ACS Appl. Mater. Interfaces*, 2021, **13**, 40379–40391.
25 J. Schindelin, I. Arganda-Carreras, E. Frise, V. Kaynig, M. Longair, T. Pietzsch, S. Preibisch, C. Rueden, S. Saalfeld and B. Schmid, *Nat. Methods*, 2012, **9**, 676–682.
26 L. Amato, S. S. Keller, A. Heiskanen, M. Dimaki, J. Emnéus, A. Boisen and M. Tenje, *Microelectron. Eng.*, 2012, **98**, 483–487.
27 K. L. Ly, S. A. Rooholghodos, C. Rahimi, B. Rahimi, D. R. Bienek, G. Kaufman, C. B. Raub and X. Luo, *Biomed. Microdevices*, 2021, **23**, 1–11.
28 W. Liu, L. Li, X. Wang, L. Ren, X. Wang, J. Wang, Q. Tu, X. Huang and J. Wang, *Lab Chip*, 2010, **10**, 1717–1724.
29 T. Agarwal, G. H. Narayana and I. Banerjee, *Cytoskeleton*, 2019, **76**, 209–218.
30 K. D. Peck, A. H. Ghanem and W. I. Higuchi, *Pharm. Res.*, 1994, **11**, 1306–1314.
31 M. Park, S. Islam, H. E. Kim, J. Korostoff, M. B. Blatz, G. Hwang and A. Kim, *Adv. Healthcare Mater.*, 2020, **9**, 2000658.
32 L. A. Low, C. Mummery, B. R. Berridge, C. P. Austin and D. A. Tagle, *Nat. Rev. Drug Discovery*, 2021, **20**, 345–361.
33 A. Guan, P. Hamilton, Y. Wang, M. Gorbet, Z. Li and K. S. Phillips, *Nat. Biomed. Eng.*, 2017, **1**, 1–10.
34 A. P. M. Guttenplan, Z. Tahmasebi Birgani, S. Giselbrecht, R. K. Truckenmüller and P. Habibović, *Adv. Healthcare Mater.*, 2021, **10**, 2100371.
35 G. A. Van Norman, *JACC: Basic Transl. Sci.*, 2019, **4**, 845–854.
36 J. Seok, H. S. Warren, A. G. Cuenca, M. N. Mindrinos, H. V. Baker, W. Xu, D. R. Richards, G. P. McDonald-Smith, H. Gao and L. Hennessy, *Proc. Natl. Acad. Sci. U. S. A.*, 2013, **110**, 3507–3512.
37 N. Dhiman, P. Kingshott, H. Sumer, C. S. Sharma and S. N. Rath, *Biosens. Bioelectron.*, 2019, **137**, 236–254.
38 R. Dong, Y. Liu, L. Mou, J. Deng and X. Jiang, *Adv. Mater.*, 2019, **31**, 1805033.
39 J. H. Tsui, W. Lee, S. H. Pun, J. Kim and D.-H. Kim, *Adv. Drug Delivery Rev.*, 2013, **65**, 1575–1588.
40 S. S. Socransky and A. D. Haffajee, *J. Periodontol.*, 1992, **63**, 322–331.
41 L. Niu, H. Zhang, Y. Liu, Y. Wang, A. Li, R. Liu, R. Zou and Q. Yang, *ACS Biomater. Sci. Eng.*, 2019, **5**, 4844–4851.
42 C. M. França, A. Tahayeri, N. S. Rodrigues, S. Ferdosian, R. M. P. Rontani, G. Sereda, J. L. Ferracane and L. E. Bertassoni, *Lab Chip*, 2020, **20**, 405–413.
43 C. Rahimi, B. Rahimi, D. Padova, S. A. Rooholghodos, D. R. Bienek, X. Luo, G. Kaufman and C. B. Raub, *Biomicrofluidics*, 2018, **12**, 054106.
44 N. S. Rodrigues, C. M. França, A. Tahayeri, Z. Ren, V. P. Saboia, A. J. Smith, J. L. Ferracane, H. Koo and L. E. Bertassoni, *J. Dent. Res.*, 2021, **100**, 1136–1143.
45 L. Palomo and G. T. Terézhalmy, *Provider*, 2014, **501**, 211886.
46 P. Rosen, D. Clem, D. L. Cochran, S. Froum, B. McAllister, S. Renvert and H. L. Wang, *J. Periodontol.*, 2013, **84**, 436–443.
47 S. Sakka, K. Baroudi and M. Z. Nassani, *J. Investig. Clin. Dent.*, 2012, **3**, 258–261.
48 G. Charalampakis, Å. Leonhardt, P. Rabe and G. Dahlén, *Clin. Oral Implants Res.*, 2012, **23**, 1045–1054.
49 X. Li, N. Wu, Y. Rojanasakul and Y. Liu, *Sens. Actuators, A*, 2013, **193**, 186–192.
50 E. W. Young and D. J. Beebe, *Chem. Soc. Rev.*, 2010, **39**, 1036–1048.

51 K. Microchem, *Kayaku Microchem*, 2019.
52 S. K. Sia and G. M. Whitesides, *Electrophoresis*, 2003, **24**, 3563–3576.
53 R. J. Lanzafame, I. Stadler, A. F. Kurtz, R. Connelly, P. Brondon and D. Olson, *Lasers Surg. Med.*, 2007, **39**, 534–542.
54 M. R. Hamblin, *AIMS Biophys.*, 2017, **4**, 337.
55 Y.-H. Hsu, Y.-F. Lin, C.-H. Chen, Y.-J. Chiu and H.-W. Chiu, *J. Mol. Med.*, 2017, **95**, 1203–1213.
56 Q. Sun, H.-E. Kim, H. Cho, S. Shi, B. Kim and O. Kim, *J. Photochem. Photobiol., B*, 2018, **186**, 31–40.